JOURNAL OF THE MECHANICAL BEHAVIOR OF BIOMEDICAL MATERIALS 39 (2014) 375–390

Available online at www.sciencedirect.com

ScienceDirect

www.elsevier.com/locate/jmbbm

Research Paper

Mechanical assessment of grit blasting surface treatments of dental implants

*K. Shemtov-Yona**, *D. Rittel*, *A. Dorogoy*

Faculty of Mechanical Engineering, Technion, Israel Institute of Technology, 32000 Haifa, Israel

ARTICLE INFO

Article history:
Received 2 June 2014
Received in revised form
20 July 2014
Accepted 28 July 2014
Available online 11 August 2014

Keywords:
Dental implants
Surface treatment
Failure analysis
Retrieved dental implants
Surface topography
Grit blasting
Finite element analysis

ABSTRACT

This paper investigates the influence of surface preparation treatments of dental implants on their potential (mechanical) fatigue failure, with emphasis on grit-blasting. The investigation includes limited fatigue testing of implants, showing the relationship between fatigue life and surface damage condition. Those observations are corroborated by a detailed failure analysis of retrieved fracture dental implants. In both cases, the negative effect of embedded alumina particles related to the grit-blasting process is identified. The study also comprises a numerical simulation part of the grit blasting process that reveals, for a given implant material and particle size, the existence of a velocity threshold, below which the rough surface is obtained without damage, and beyond which the creation of significant surface damage will severely reduce the fatigue life, thus increasing fracture probability.

The main outcome of this work is that the overall performance of dental implants comprises, in addition to the biological considerations, mechanical reliability aspects. Fatigue fracture is a central issue, and this study shows that uncontrolled surface roughening grit-blasting treatments can induce significant surface damage which accelerate fatigue fracture under certain conditions, even if those treatments are beneficial to the osseointegration process.

1. Introduction

Dental implants offer a highly successful solution for missing teeth, contingent upon the well-known osseointegration process. Albrektsson et al. (1981) stated that the implant's surface properties affect the successful course of osseointegration. Those properties can be addressed from three different directions: Mechanical, topographic, and physicochemical (Albrektsson and Wennerberg, 2004).

The effect of surface topography on the biological reaction and on bone-implant contact has been studied extensively in the dental implant research field, for over a decade. Average height deviation parameters (R_a and S_a) between 1 and 2 μm, which define a "moderately rough surface", were found to be optimal for a successful osseointegration process (Albrektsson and Wennerberg, 2004; Elias and Meirelles, 2010; Wennerberg and Albrektsson, 2009, 2010).

A great variety of surface treatments exist today, in order to achieve a desired degree of surface roughness. Those include machining, plasma spray and laser peening (LST), acid etching, grit blasting followed by acid etching, anodizing and biomimetic coating. Among those, grit blasting is one of

*Corresponding author.
E-mail address: kerenrst77@gmail.com (K. Shemtov-Yona).

http://dx.doi.org/10.1016/j.jmbbm.2014.07.027
1751-6161/

the most common dental implant surface treatments (Elias and Meirelles, 2010; Wennerberg and Albrektsson, 2010). Blasted surface roughness with S_a values ranging from 0.6 and 2.1 μm is deemed ideal for the implant's osseointegration (Wennerberg and Albrektsson, 2009). During this process, implants made of pure titanium (CP–Ti) and titanium alloy (Ti–6Al–4V) – which are the most widely used biomaterials for fabrication of dental implants (Elias et al., 2008) – are blasted with air – propelled hard ceramic particles (Al_2O_3, TiO_2 or $Ca_2P_2O_7$) (Guéhennec et al., 2007). Depending on the size and shape of the ceramic particle, which is polyhedral with sharp corners (Barriuso et al., 2014), and on its velocity, erosion and material tearing of the titanium surface, is inflicted. The result is different surface roughness levels that can be produced on the implant's surface.

While the biological benefit of such surface treatment has become a paradigm in the field of dentistry, the *mechanical properties* of the implant surfaces have not been thoroughly studied yet, and researches dealing with the effect of the surface treatment on the implant's mechanical behavior are still scarce.

Late treatment complications in implant dentistry include mechanical failures. Those consist of abutment screw loosening, abutment screw fracture, implant's abutment fracture and *implant fracture*. Implant and implant components fracture are considered severe in dentistry, because they often necessitate extra surgery, and lead to the loss of implants and loss of the prosthesis supported by the implants. Pjetursson et al. (2012) reported an incidence of implants (and parts) fracture of the order of only 0.5%, after a follow up time of at least 5 years. Pommer et al. (2014) recently published a meta-analysis on the incidence of implants' fracture, reviewing clinical studies that reported such fractures. Their study concluded that the incidence of implant fracture jumps to 2.8% after a follow up time of 8.3 years. Most fractured implant included in this study, occurred just after 4.1 ± 3.5 years. These incidences clearly highlight the *importance of follow up time* on the occurrence of implant fracture. Here, the concept of "bathtub curve" which is quite central in reliability engineering should apply to dental implants as well. This concept shows that failure occurs largely over the first short period of life of a component (e.g. infant mortality), settles down to a low level (service time), then finally rises dramatically towards the end of the product's life (Henley and Kumamoto 1981). One could therefore surmise that the studied period of less than 10 years, for the specific fracture of implants, *is most likely located in the bottom of the bathtub curve* (See Pjetursson et al., 2012; Pommer et al., 2014). Thus, in order to prevent future implant fracture, it is important to identify the relevant physical and mechanical causes. This point should be clearly understood, since the current paradigm, which states that implant fracture is a rare exception, is mostly based on an extrapolation of results valid over 5 years to much longer periods, with the inherent error related to the very concept of data extrapolation. All the more so, when *fatigue fracture* (the main identified fracture mechanism) amounts to damage accumulation over time, as discussed in the sequel.

Detailed failure analyses of retrieved fractured dental implants are quite rare in the dental and in the biomechanical literature alike. Most fractured implants are left in the alveolar bone after fracture because of the difficulty to retrieve them. In most cases, the fracture surface of the implants, which is essential for fracture analysis, is destroyed or heavily damaged to a point that renders fractographic analysis impossible. A few published articles (Choe et al., 2004; Morgan et al., 1993; Sbordone et al., 2010; Shemtov-Yona and Rittel, 2014; Yokoyama et al., 2002), that examined the fracture surface of retrieved fractured dental implants, identified the probable causes leading to mechanical failure. Most studies (Choe et al., 2004; Morgan et al., 1993; Sbordone et al., 2010) identified *metal fatigue* (Suresh 1994) as the main failure mechanism. As opposed to the crack growth mechanism, the cause(s) for fatigue crack initiation and the crack nucleation site(s) *could not be clearly identified*.

With that, *implant design* that includes significant stress concentrators (Morgan et al., 1993) can be incriminated. In addition, large dents and scratches, with foreign particles, introduced during the *manufacturing process*, have also been considered as another cause for fatigue crack initiation (Choe et al., 2004; Yokoyama et al., 2002). All those are surface defects.

Fatigue properties of metals are largely affected by surface condition/topography, since fatigue cracks generally initiate from free surfaces. The presence of notch-like surface irregularities *related to machining and surface treatments*, may have a deleterious effect on fatigue crack initiation and on the total fatigue life. In addition, embedded particles and/or particles adhered to the surface, combined with high surface roughness, might induce stress concentrations and significantly degrade the metal fatigue performance (Novovic 2004). Examination of treated CP–Ti or titanium alloy by scanning electron microscopy reveals the aggressive effect of the blasting treatment. The treated metal surface is rough, as expected, but it may also comprise multiple notch-like superficial defects. These defects are the evidence of erosion and material tearing caused by the sharp edges of the ceramic particles. Moreover, firmly embedded ceramic particles can also be found attached to a crater-like morphology which they have created (Leinenbach and Eifler, 2006; Multigner et al., 2009; Pazos et al., 2010). These particles sometimes cause very fine cracks in their immediate vicinity (Barriuso et al., 2011; Conforto et al., 2004). All those evidences are certainly detrimental to the long-term mechanical performance of the implants.

The effect of grit blasting treatments on the fatigue performance of *titanium and titanium alloys* was studied in several instances. Baleani et al. (2000) showed that grit blasting of Ti6Al4V can reduce the fatigue endurance limit by 35–40%. The authors incriminated the surface roughness and the sharp defects created by the treatment. Conversely, Pazos et al. (2010) reported that the fatigue behavior of blast-treated and machined CP–Ti surface is similar, in spite of the inherent stress raisers related to the alumina particles. The authors invoked the beneficial effect of blasting induced compressive residual stresses that balanced the negative effect of the stress raisers. Leinenbach and Eifler (2006) compared the fatigue performance of grit blasted and polished Ti–6Al–4V cylindrical specimens. The results showed that the endurance limit of the grit blasted material

was decreased by 25%. Scanning electron (SEM) characterization revealed the formation of microcracks in the vicinity of the embedded alumina particles. Multigner et al. (2009) investigated grit-blasted Ti–6Al–4V, and their conclusion was that surface defects induced by the process are responsible for the observed degradation of the fatigue limit. However, all the above-mentioned studies did not consider the parameters of the grit-blasting treatment per-se.

To summarize the main issues mentioned with the introduction, it appears that while grit blasting surface treatments may be beneficial to the clinical and (perhaps) mechanical survivability of dental implants, they may as well significantly degrade the surface of the implants in the context of fatigue fractures. Let us emphasize that this work does not investigate surface roughness per-se, but the focus is on potential damage inflicted to the implant's surface and its implications in future mechanical failure.

Therefore, one open question remains to be addressed, namely can one identify parameters of the grit blasting treatment that harm the fatigue performance of dental implants?

This investigation includes laboratory fatigue testing of commercial Ti–6Al–4V dental implants. It also includes a detailed failure analysis of retrieved fractured dental implants made of CP–Ti and Ti–6Al–4V collected at random from the oral cavity. The investigation is supplemented with 3D finite element simulations of impact of alumina spheres on CP–Ti and Ti–6Al–4V surfaces. Those simulations mimic the grit blasting treatment, and shed light on the effect of the surface treatment, its characteristics (particle impact velocity), and the potential for future mechanical failure.

2. Materials and methods

2.1. *Laboratory testing of new commercial Ti–6Al–4V dental implants*

Nine new specimens, of the same *commercial* dental implants made of Ti–6Al–4V were tested in this study. The tapered implants were 13 mm long, with an outer diameter 3.75 mm at implant neck (Fig. 1A), and a straight 8 mm implant abutment (Fig. 1C) that was connected to the implant with an abutment screw of 7 mm long (Fig. 1B). The components were tightened with a clinical torque driver to 30 Ncm.

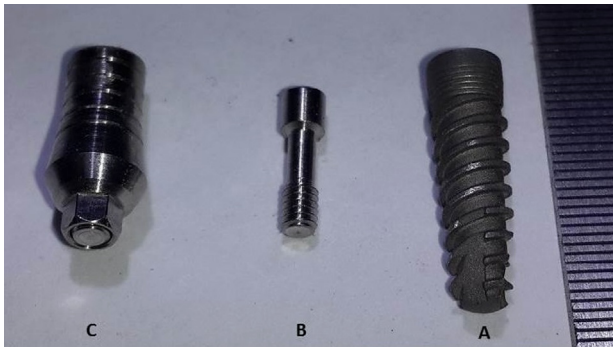

Fig. 1 – Tested implants and implant's parts. A: Implant body. B: Abutment screw. C: Implant abutment.

All the mechanical laboratory tests were carried out in room air on an MTS servo-hydraulic load frame, under load-control, according to the recommendations of ASTM (ISO 14801, 2007). Additional details and test configuration can be found in Shemtov-Yona et al. (2014a,b), and in Appendix A.

2.1.1. *Static bending test*

Five specimens were tested quasi-statically in order to test the quasi-static bending strength of the specimens, and to select the fatigue loads applied during the subsequent fatigue tests. A vertical load was applied at a displacement rate of 0.4 mm/min until the sample fractured, or exhibited a significant amount of (permanent) plastic deformation until a load drop was recorded. The average failure (peak) load was found to be of 930 ± 77 N (Shemtov-Yona et al., 2014a,b).

2.1.2. *Identification of fatigue crack initiation in commercial dental implants*

Previous fatigue test assessed the fatigue strength of 3.75 mm diameter implants through the construction of S–N curve. For those implants, the fatigue limit was found to be around 600 N (Shemtov-Yona et al., 2014a). Four additional identical implants were tested in this work. It is important to note that, whereas the implants are all identical to those previously tested and manufactured by the same manufacturer, the current *batch* was different from the previously tested batch of specimens. The fatigue load selected for the tests was set to 610 N that is 65% of the specimens' static failure load (Shemtov-Yona et al., 2014a). In order to identify crack formation, the fatigue test was divided into check-points. Each check-point corresponded to 5000 cycles. After each check-point, the testing machine was stopped and the specimen was examined in the SEM to detect cracks. The test was then continued until the next check-point, and so forth until fracture. The total number of cycles to final fracture was recorded.

2.2. *Failure analysis of retrieved fractured dental implants*

Eighteen retrieved fractured dental implants were *randomly* collected from private dental clinics. No medical record or specific information about the implant and its manufacturer were made available. Consequently, the broken parts were investigated on purely technical grounds without addressing the related medical issues.

The retrieved implants were cleaned from debris of bone and organic materials before the examination. Debris of bone were removed using EDTA solution (Ethylenediaminetetraacetic acid, chelating agent, sequester metal ions such as Ca^{2+} and Fe^{3+}). Debris of organic materials was removed using commercially pure acetone.

A total number of 10 CP–Ti and 8 Ti–6Al–4V retrieved dental implants were thus identified using SEM-EDX Energy Dispersive X-ray Analysis (EDX).

2.3. *Numerical model*

The impact of alumina spheres on plates made of CP–Ti and Ti–6Al–4V was modeled using the finite element technique. Modeling was carried out in order to shed light on the

particle-substrate interaction. Emphasis was put on the characterization of the damage imparted to the plate, and the residual stress distribution due to impact of the alumina particle. The simulations are fully qualitative, aimed at clarifying physical phenomena only, without attempting to reproduce accurately a complex multiple-impact situation.

2.3.1. *Impact of alumina sphere on Ti–6Al–4V and CP–Ti blocks.*

The diameter of the alumina particle was fixed to $D=200$ μm. The particle impacts a square block made of titanium alloy (Ti–6Al–4V), or pure titanium (CP–Ti), having a width $2W=1$ mm and height $H=0.5$ mm. The simulations were carried out using a 3D explicit commercial finite elements software, (Abaqus/CAE, 2012). The model geometry is shown in Fig. 2.

A 3D adiabatic explicit analysis was conducted, based on the fact that for short impact times, heat conduction can be neglected to a first extent. The duration of the numerical analysis was 3 μs, which is more than sufficient to show the impact and its consequences. An initial downwards velocity in the range $V_i=50$–250 m/s was imparted to the alumina sphere. Due to the symmetry of the problem, only one quarter of the assembly was modeled (Fig. 3A) with appropriate boundary conditions. The meshed quarter model is shown in Fig. 3B. The element size of the meshed sphere and the contact and penetration region of the block were 5–10 μm. The general contact algorithm of Abaqus/CAE (2012) was used with element-based surfaces that can adapt to the exposed surfaces of failed elements. Abaqus frictional tangential behavior with the penalty formulation was adopted. A coefficient of friction 0.5 was used. The material models and failure criteria used for Ti–6Al–4V, CP–Ti, and alumina are fully detailed in the Appendix section (B).

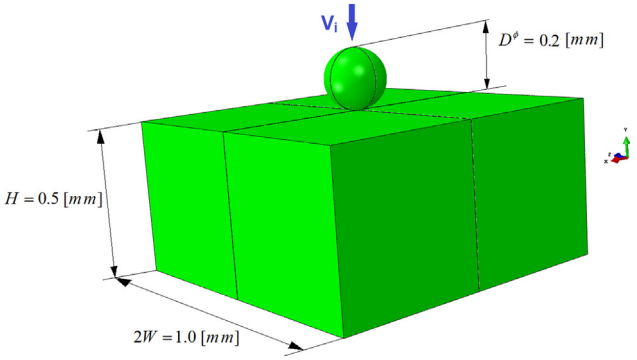

Fig. 2 – The simulated geometry.

3. Results

3.1. *Experimental*

3.1.1. *Fatigue testing of new commercial Ti–6Al–4V implants*

3.1.1.1. Surface examination of the implants prior to testing. Prior to fatigue testing, the implants' surface was examined using the SEM, as shown in Fig. 4. The macrographs are taken from the threaded parts of one of the new tested commercial implants.

At small magnification (Fig. 4A), one can note that the implant's surface is rough, as expected for improved osseointegration. However, large areas are covered by small white particles. Fig. 4B, confirms the previous observations at higher magnification. The surface is irregular and rough with large crater-like areas, with sharp edges that result of plastic deformation and material tearing. Micro-holes (pit-like surface topography) are present in those craters, which are characteristic of the acid etching surface treatment (Fig. 4C and D). Embedded particles with different sizes and shapes are scattered randomly all over the surface. Note that the implants usually undergo a cleaning procedure after the grit-blasting process, so that the observed particles survived the treatment, implying a firm bonding to the substrate. Fig. 4C and D shows that these particles, marked by red arrows, are attached to the crater like morphology that they have created. Fine small cracks 15–25 μm long (yellow arrows), which were generated in the vicinity of the particles, are observed.

3.1.1.2. Fatigue testing – Identification of fatigue cracks. Table 1 summarizes the number of check-points done until crack identification and the total number of cycles until final failure for the 4 investigated implants.

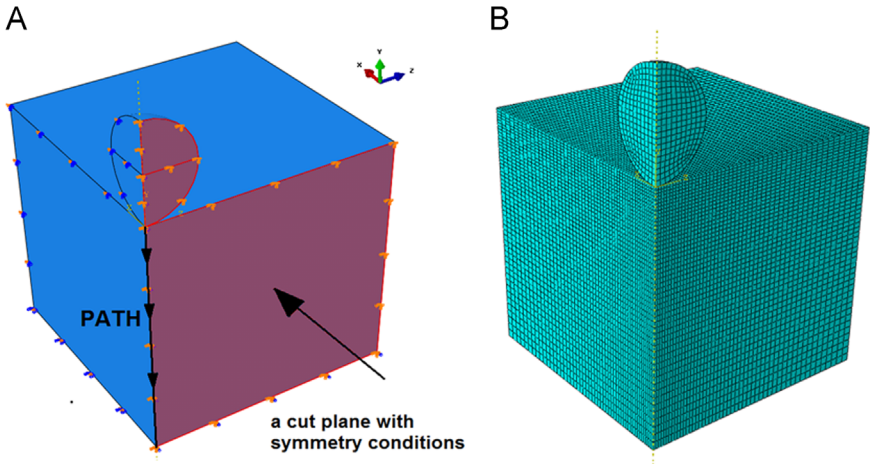

Fig. 3 – The quarter model which was simulated. A: A symmetry plane. B: The mesh.

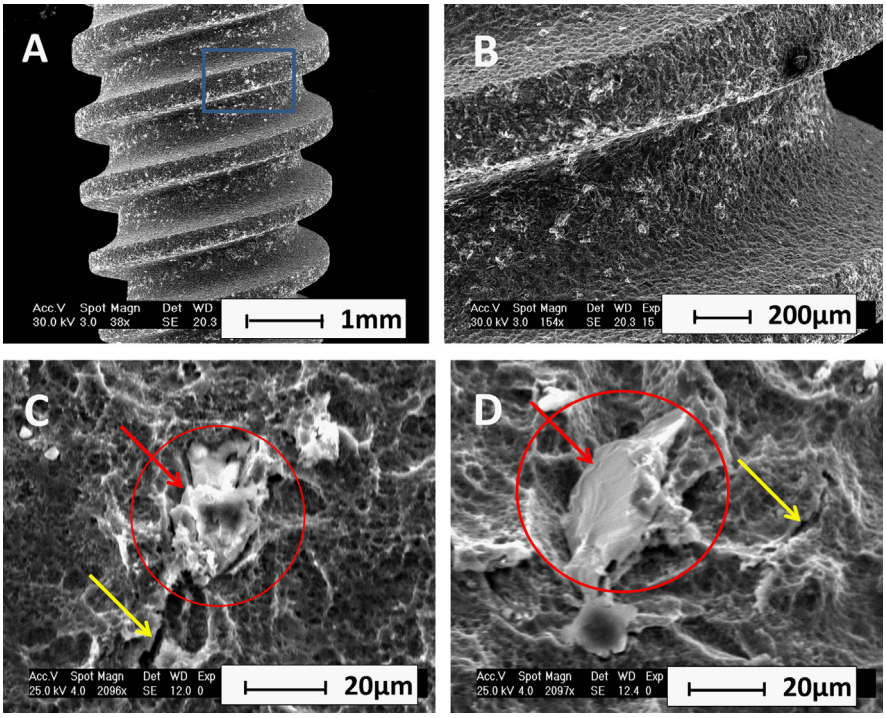

Fig. 4 – SEM macrograph of the tested commercial implants. A: Implant threads macrograph B: implant surface macrograph – the macrograph is a magnification of the area marked by a blue square on A. C and D: Embedded particle (red arrow) in a crater like area (red circle) with small cracks (yellow arrow) on the implant surface. (For interpretation of the references to color in this figure legend, the reader is referred to the web version of this article).

Table 1 – Identification of fatigue crack initiation test results. The table describes, for each tested specimen, the results of the examination of each check point that corresponds to 5000 cycles. The [−] symbol indicates that at this check point a crack was not identified by using SEM. The [+] symbol indicates that a crack was identified at this stage. The total number of cycles until final failure is indicated.

Implant #	Check points (no. of cycles) 1 (5000)	2 (10000)	3 (15000)	4 (20000)	Cycles until total failure
1	NA	NA	NA	NA	4508
2	−	−	+	NA	15205
3	−	−	+	NA	19850
4	−	−	−	+	36004

The fatigue test shows that, on the 4 tested specimens, cracks were identified between check-points 3 and 4, meaning they most likely nucleated in the interval of 10,000–15,000 cycles. This total number of cycles to failure is *extremely low*, compared to our previous measurements for which similar cases corresponded to a 90% probability of survival (i.e $N > 5 \times 10^6$ cycles)! This point will be further discussed and clarified since it is quite central to this work. At this stage, let us reiterate that the tested specimens are identical to all the previously tested ones, except for the fact they come from a different batch. The current tests revealed an additional point, namely that the incremental number of cycles to final failure, once a crack was identified on the implant surface, is extremely low, of the order of 7000 cycles. This observation just points to the fact that crack propagation is rapid in those tests.

Fig. 5 is a SEM surface micrograph of cracks observed on specimen #3 after 3 check-points (15,000 cycles) *before the final fracture*. Such micrographs are representative of all the tested specimens. In all cases, a large main crack was identified. The crack was located between the second and third threads of the implant. Fig. 5A–D shows details of that crack. Lateral secondary cracks, branched from the large main crack, can be identified (Fig. 5 yellow arrows). In addition, Fig. 5A D shows that large and small embedded particles (red arrows) are located along the cracks paths, and probably dictated it.

Next, we examined the fracture surface of specimen #3 *after final fracture*. Two regions can be identified. The main region is rough with sharp edges that fill about 90% of the fracture surface (Fig. 6A letter O). This region correspond the ductile overload failure, with dimples (Kerlins and Phillips, 1987) at magnification of 1K (not shown in the figure). The second region is flat and fills only 10% of the fracture surface (Fig. 6A letter F). This region corresponds to the fatigue failure process with its classical striations (Kerlins and Phillips, 1987), at magnification of 7K (not shown in the figure). The fatigue crack initiation site is marked by blue arrow on the fractograph, as identified from the array of steps (outlined by a

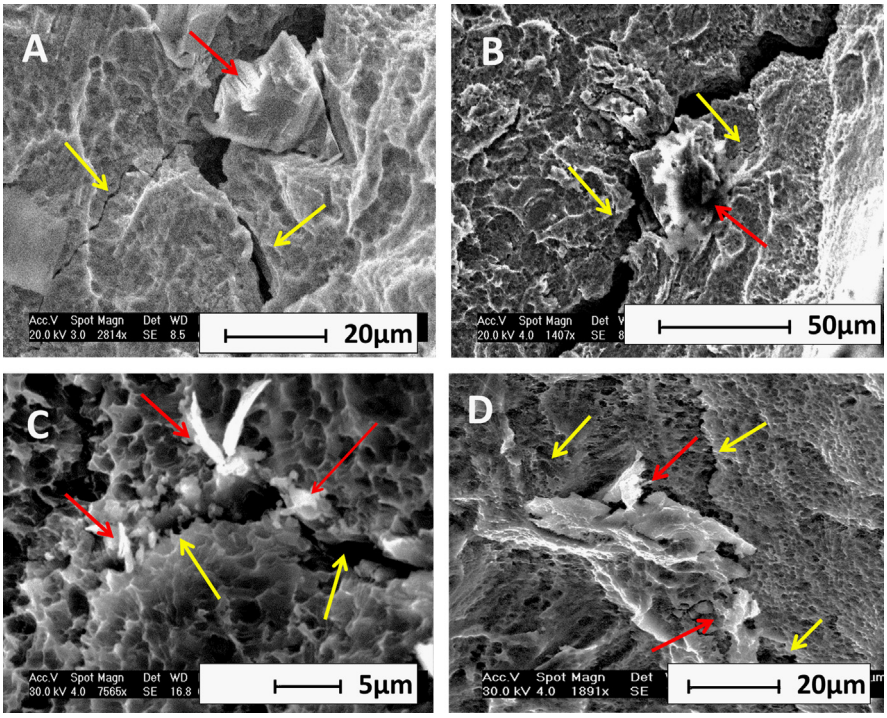

Fig. 5 – A–D: SEM micrograph of crack identification on fatigue tested specimen 3 before the final failure. On each micrograph the large main cracks and lateral secondary cracks can be identified (yellow arrows) embedded along the cracks are ceramic particles (red arrows). (For interpretation of the references to color in this figure legend, the reader is referred to the web version of this article).

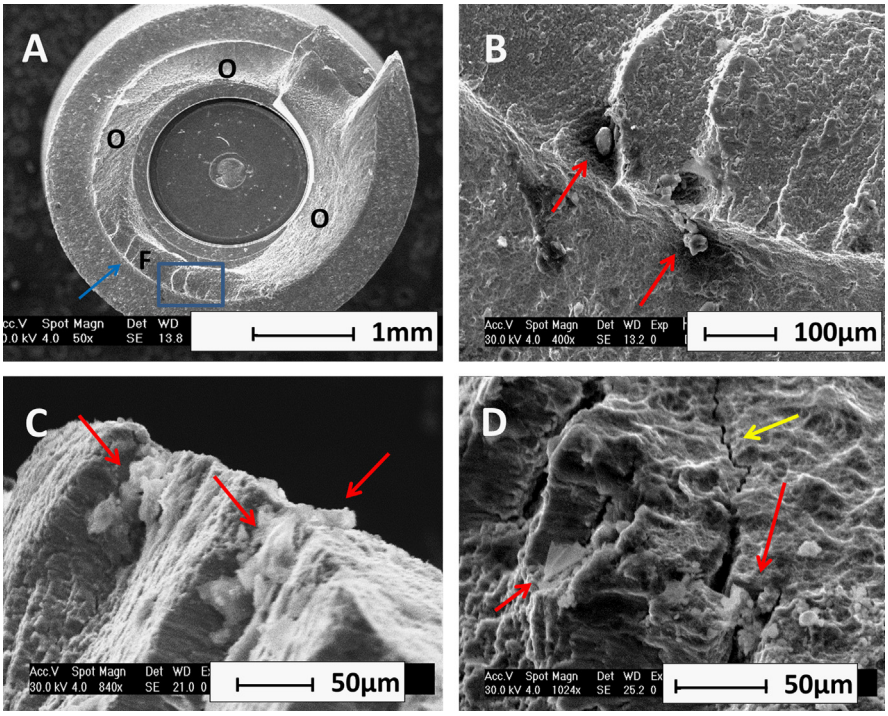

Fig. 6 – Fracture surface of fatigue tested implant after final fracture. A: The fracture surface with flat part caused by fatigue failure mechanism marked by the letter "F" with crack initiation location (Blue arrow) and rough part marked by the letter "O" B: Upper view of crack initiation location – the macrograph is an enlargement of the area marked by a blue square on A with embedded particles marked by red arrows C: Side view of crack initiation location with embedded particles marked by red arrows. D: Side view: secondary cracks, marked by yellow arrows, on the lateral view, at the vicinity of the fracture surface with embedded particles along the crack, marked by red arrow. (For interpretation of the references to color in this figure legend, the reader is referred to the web version of this article).

rectangle in Fig. 6A). This region is magnified in Fig. 6B. The presence of foreign particles (red arrows) embedded in, or close to the steps is clearly visible.

Looking at the outer face of each staircase from the surface side (side view), shows again embedded particles (Fig. 6C red arrows). All the above fractographic evidence suggests that the ceramic particles are related to the cracks nucleation sites, leading to final fracture. Lateral secondary cracks can be identified on side views of the implant surface, near the outer face of the fracture surface, (Fig. 6D yellow arrows) with embedded particles (Fig. 6D red arrows).

3.1.2. *Fractographic analyses of retrieved CP–Ti and Ti–6Al–4V dental implants*

Fig. 7 (Ti–6Al–4V) and 8 (CP–Ti) show typical fractographs obtained during the failure analysis that was carried out in order to identify the failure mechanism(s). The fracture surfaces are all outlined by a circle. The fracture surface can be divided into two regions, as was observed for the laboratory specimens. The main part is flat and unified in appearance and occupies roughly 90% of the fracture surface. The second region is rough with sharp edges over the remaining 10% of the fracture surface. The operating failure mechanism in the first region is identified as (ductile) monotonic overload, as evidenced from the dimples observed in this region (Figs. 7D and 8D).

On the fracture surface of retrieved fractured CP–Ti and Ti–6Al–4V dental implants, parallel lines were identified and marked by the letter B in Figs. 7A and 8A. Those parallel lines can be seen at higher magnification in Figs. 7B and 8B. Such lines are identical in nature to those identified on the fracture surfaces of the laboratory fatigue tested implants (Fig. 6A and B). Consequently, those features point to the origin of the fatigue crack, i.e. the onset of the implant's failure process (Figs. 7B and 8B). In this case too, the lines originate from the free surface of the implants.

Fractographic examination of the flat region, for every examined retrieved dental implant, clearly reveals the operation of a *fatigue fracture mechanism*. Faint fatigue striations (Kerlins and Phillips, 1987; Shemtov-Yona et al., 2014b) are observed on the retrieved Ti–6Al–4V dental implants when high magnification of 10K is used (Fig. 7C green arrow). These fatigue striations were identical to the fatigue markings seen on the specimen fractured in lab conditions. Likewise, clear fatigue striations are visible on the retrieved CP–Ti dental implants when a magnification of 6K or more is used (Fig. 8C, green arrow).

The rough part of the fracture surface marked by the letter D on Figs. 7A and 8A is characteristic of monotonic ductile overload failure (Kerlins and Phillips, 1987).

While strong similarities can be noted concerning the fractographic features, the *surface* topography of each retrieved fractured implant is unique and characteristic. This is deemed to be the result of the different surface treatments aimed at roughening their surface. When the surface of the implant is examined, numerous secondary cracks are observed. Fig. 9 shows surface micrographs of secondary cracks from four retrieved fracture dental implants made of

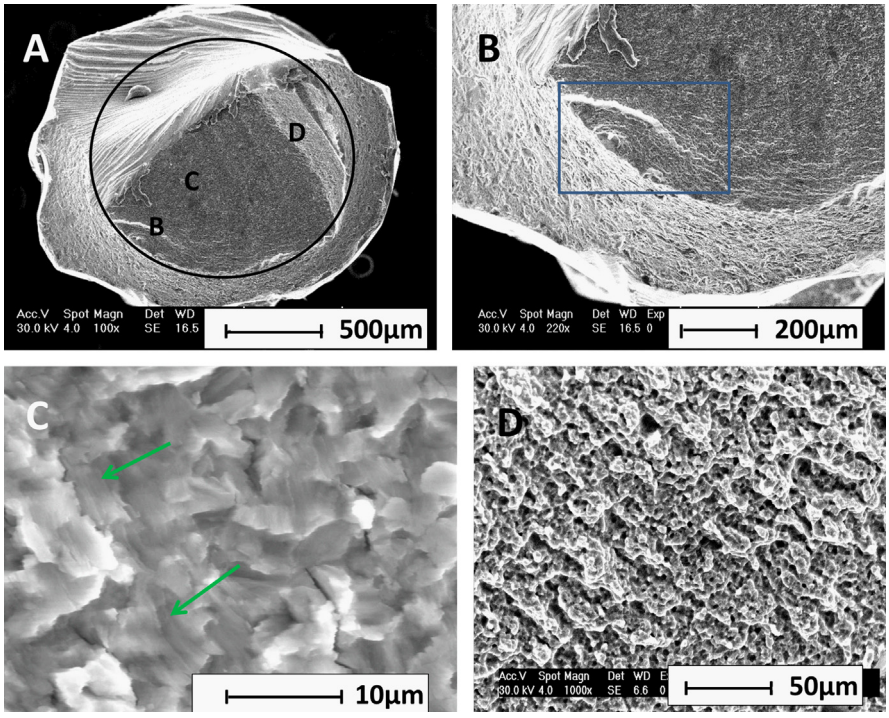

Fig. 7 – Failure analysis of retrieved fractured Ti–6Al–4V dental implants with representative fractographs A: The fracture surface marked by round circle. The letters on the fracture surface are the locations on the fracture surface of fractographs B, C and D. B: fractograph of crack initiation location (Blue square) (X220). C: fractograph of fatigue crack propagation: fatigue striations are marked by green arrows (8 K) on the flat part. D: final failure markings, dimples on the rough part. (For interpretation of the references to color in this figure legend, the reader is referred to the web version of this article).

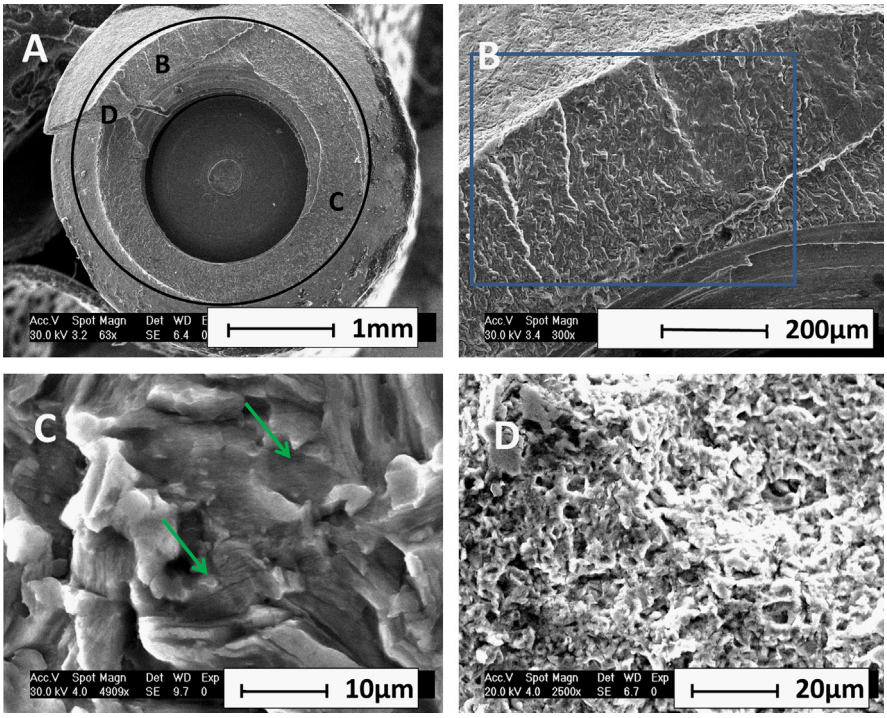

Fig. 8 – Failure analysis of retrieved fractured CP–Ti dental implants with representative fractographs A: The fracture surface marked by round circle. The letters on the fracture surface are the locations on the fracture surface of fractographs B, C, and D. B: fractograph of crack initiation location. Parallel line marked by a blue square on the flat part. C: fractograph of fatigue crack propagation: fatigue striations are marked by green arrows on the flat part. D: final failure markings, dimples on the rough part. (For interpretation of the references to color in this figure legend, the reader is referred to the web version of this article).

TI–6Al–4V (Fig. 9 A and B) and CP–Ti (Fig. 9C and D). These micrographs are taken from the threaded part of the implant's body.

SEM micrographs of the secondary cracks in several retrieved Ti–6Al–4V and CP–Ti implants, show embedded foreign particles (Fig. 9 red arrows). EDX analysis of the embedded particles on the path of the secondary cracks reveals that these particles are made of Al_2O_3 and/or FeO. Judging from the overall secondary crack path, it appears that the embedded particles affect the secondary crack path itself.

3.1.3. *Summary of the experimental results*

To summarize, our experimental results have clearly shown how surface cleanliness and topography have a major effect on mechanical durability of dental implants.

For lab-tested implants, their surface *before implantation* is likely to be heavily contaminated with ceramic particles embedded on the surface. These particles are the result of the surface treatment that leaves the titanium surface rough with deep craters and embedded particles. The effect of the treatment on the mechanical durability of the implants is deleterious, in the sense that such a surface condition will lead to an accelerated fatigue crack initiation and rapid failure.

Those observations are further corroborated by the examination of fractured implants retrieved from the oral cavity. Here too, the fatigue crack nucleation can be unambiguously traced back to various stress raisers, among which embedded ceramic particles. In other words, lab-induced failures can be considered as highly representative of intraoral-cavity failures.

3.2. *Numerical results*

3.2.1. *Residual pressure distribution*

Impact of particles with initial velocities of 50–250 m/s, in steps of 50 m/s, was simulated for the two plate materials, Ti–6Al–4V and CP–Ti grade 1. The residual three-dimensional (3D) pressure distribution $(P = \sigma_{ii}/3)$ at t=2.5 µs, i.e. long after the transient impact effects, is shown in Fig. 10. The pressure distribution for the Ti–6Al–4V plate impacted at 50 and 250 m/s is shown in Fig. 10A and C, respectively. The results for the CP–Ti impacted at similar velocities are shown in Fig. 10B and D. A large zone underneath the impact location is subjected to a residual pressure (stress) because of the large plastic deformation of the substrate. A crater is formed underneath the impact location, as shown in Fig. 10A and B, even at the lower impact velocity of 50 m/s for both materials. The dimensions (depth and diameter) of the crater grow with increasing impact velocity. Both materials break and tear for impact velocities higher than 150 m/s, as shown in Fig. 10C and D.

It thus appears that for a specific the investigated systems (particle and target), there is a *threshold impact velocity* (V_{th}). This threshold is of the order of 150 m/s. At lower velocities the impact of the alumina sphere induces a residual pressure within the metal surface. This comes along with the creation of a rough surface topography consisting of craters whose diameter grows

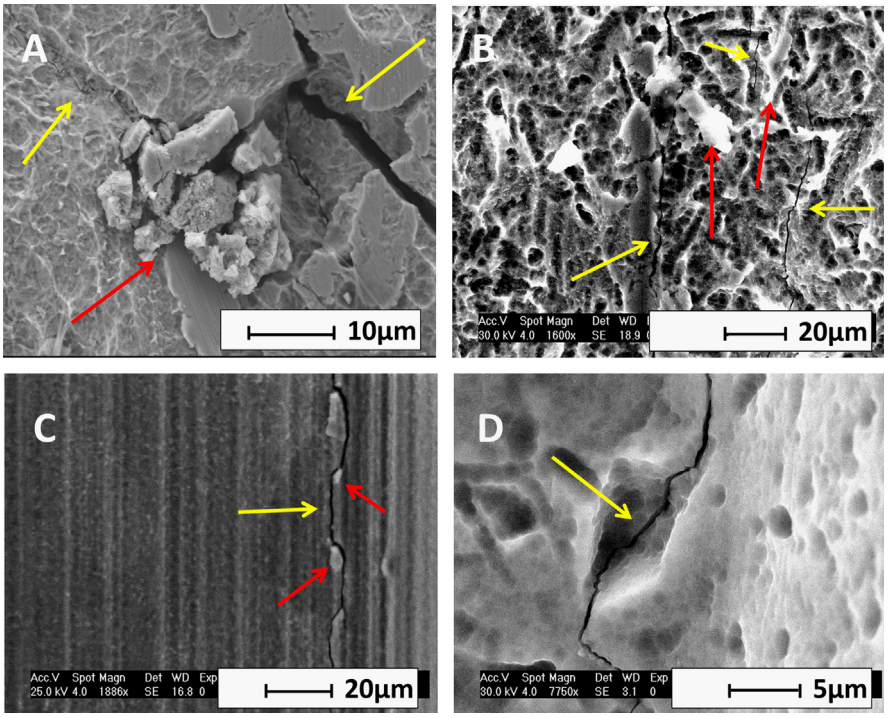

Fig. 9 – surface micrographs A and B: micrograph from Ti–6Al–4V implant's surface that were grit blasted and acid etched with secondary cracks (yellow arrow) with embedded ceramic particles along the secondary cracks path (red arrow). C: micrograph from machined implant surface with secondary cracks (yellow arrow) with embedded particles caused by machining. D: micrograph from implant surface with secondary cracks (yellow arrow) with deep craters generated by the surface treatment. The secondary crack passes through the deep crater. (For interpretation of the references to color in this figure legend, the reader is referred to the web version of this article).

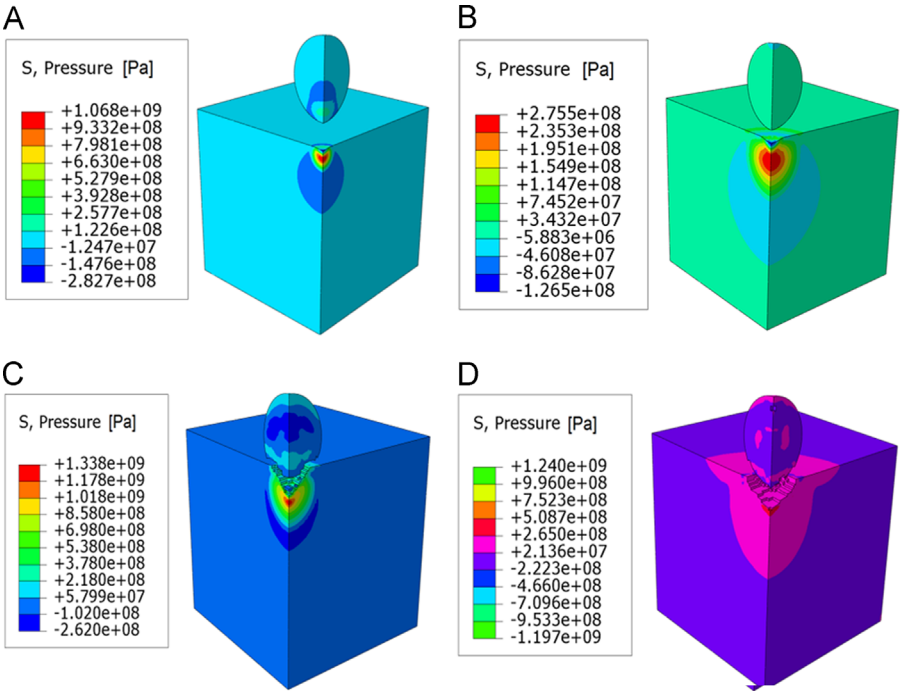

Fig. 10 – Contour maps of residual pressure due to impact. A: Ti–6Al–4V plate at 50 m/s. B: CP–Ti plate at 50 m/s. C: Ti–6Al–4V plate at 250 m/s. D: CP–Ti plate at 250 m/s. Note that the region of positive residual pressure (compression) is much larger for the CP–Ti for both impact velocities.

with the impact velocity. At velocities higher than the V_{th}, the materials break and tear.

3.2.2. *Residual strain distribution*

The residual equivalent plastic strain distribution along a vertical path is shown in Fig. 11 for impact velocities of 50, 100 and 150 m/s. The path starts at impact location and stretches to the bottom of the plate (Fig. 3A). The velocities affect the size of the region in which plastic residual strains exist and the strain distribution (shape and magnitude) within this region. A first characteristic parameter of the region is its length along the path. A second characteristic parameter, indicating the extent of the residual plastic strain within the region, is its peak value (since the distribution shape is similar for all velocities). It can be observed that the impact velocity has the same effect on the Ti–6Al–4V and the CP–Ti. Increasing the impact velocity causes the plastic region's length (along the path) to increase, and its peak values to grow. The peak value of the residual equivalent plastic strain in CP–Ti is ~50% higher than for the Ti–6Al–4V. The length of the plastic zone of the CP–Ti is ~2 times larger. Such residual strains are the essence of hardening surface treatments aimed at improving the fatigue life of a component.

3.2.3. *Damage regions in the plate*

The residual pressure distribution along the vertical path (Fig. 3A) is shown in Fig. 12. In Fig. 12A, the pressures are plotted along the path for impact velocities $V=50$, 100 and 150 m/s, for which the substrate material does not break and tear. Results for impact velocities of 200 and 250 m/s are shown in Fig. 12B, keeping in mind that at those impact velocities, the two substrate materials break and tear (Fig 10C and D).

From Fig. 12A, three regions, numbered I to III, can be identified, starting just underneath the impact, as follows:

i) A small tensile pressure region adjacent to the impacted surface.
ii) A large compression pressure region.
iii) A large tensile pressure region following the compression pressure region.

The regions are outlined for CP–Ti impacted at 150 m/s in Fig. 12A.

For the two materials, as shown in Fig. 12B, the tension region I no longer exists and is replaced instead by a zero pressure region. This is due to local fracture (ablation of material) that occurs at impact velocities exceeding 150 m/s.

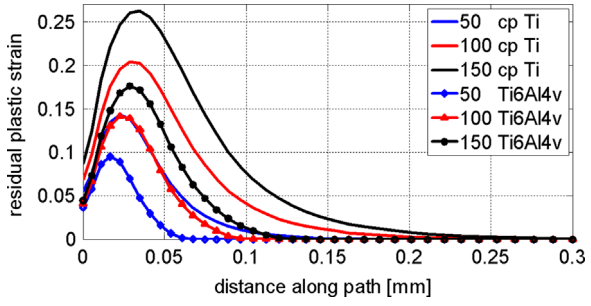

Fig. 11 – Residual equivalent plastic strain distribution along a vertical path (shown in Fig. 3A) underneath the impact location for CP–Ti and Ti–6Al–4V impacted at 50, 100 and 150 m/s.

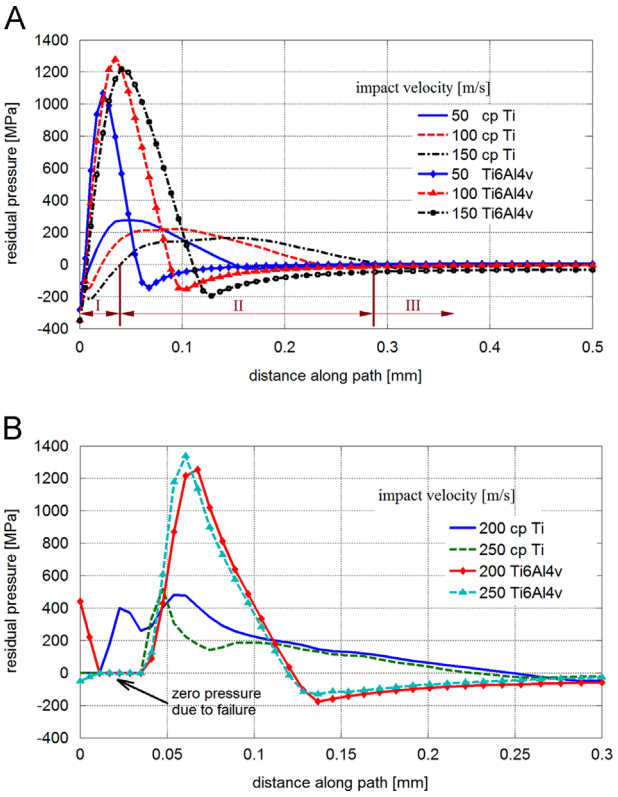

Fig. 12 – Residual pressure distribution along a vertical path (shown in Fig. 3A) underneath the impact location for CP–Ti and Ti–6Al–4V. A: impact at 50, 100 and 150 m/s. B: impact at 200 and 250 m/s.

The effect of impact velocities of 50, 150 and 250 m/s is summarized in Table 2. It can be noticed that for sub-threshold velocities of 50 and 150 m/s, the regions I and II are much wider for the CP–Ti in comparison to the Ti–6Al–4V, and they grow with the impact velocity.

For impact velocities higher than 150 m/s, region I disappears as mentioned earlier and the length of the compression region II shortens. For the Ti–6Al–4V impacted at 250 m/s, this region lies between $35[\mu m] \le l_{ii} \le 119[\mu m]$, and its length becomes 84 μm, while for a lower impact velocity of 150 m/s, it was 102 μm. For the CP–Ti impacted at 250 m/s, the same region lies between $35[\mu m] \le l_{ii} \le 225[\mu m]$, and its length becomes 190 μm, while for an impact velocity of 150 m/s it was 251 μm.

3.2.4. *Damage of the ceramic sphere*

The damage imparted to the ceramic sphere at 2.5 μs after impact with the plates at all velocities (50–250 m/s) is shown on a mid-section of the sphere in Fig. 13. The damage parameter (SDV_DAMAGE) in the JH2 model lies within 0 and 1, and quantifies the severity of the damage, from none (0) to total (1).

Fig. 13 shows that the ceramic sphere is already damaged at an impact velocity of 50 m/s when the substrate is made of Ti–6Al–4V, while with CP–Ti, damage starts only at 150 m/s.

Table 2 – Extent and peak residual pressure of the 3 regions for impact velocities for 50, 150 and 250 m/s.

	Impact velocity [m/s]	CP–Ti			Ti–6Al–4V		
		Extent [μm]	Length [μm]	Peak pressure [MPa]	Extent [μm]	Length [μm]	Peak Pressure [MPa]
Region I	50	$0 \le l_I \le 11$	11	−120	$0 \le l_I \le 4$	4	−284
	150	$0 \le l_I \le 40$	40	−217	$0 \le l_I \le 8$	8	−350
	250	–	–	–	–	–	–
Region II	50	$11 \le l_{II} \le 150$	139	275	$4 \le l_{II} \le 56$	52	1066
	150	$40 \le l_{II} \le 291$	251	163	$8 \le l_{II} \le 110$	102	1220
	250	$35 \le l_{II} \le 225$	190	517	$35 \le l_{II} \le 119$	84	1340
Region III	50	$150 \le l_{III} \le 500$	350	−27	$560 \le l_{III} \le 500$	444	−145
	150	$291 \le l_{III} \le 500$	209	−24	$110 \le l_{III} \le 500$	390	−196
	250	$2250 \le l_{III} \le 500$	275	−30	$119 \le l_{III} \le 500$	481	−126

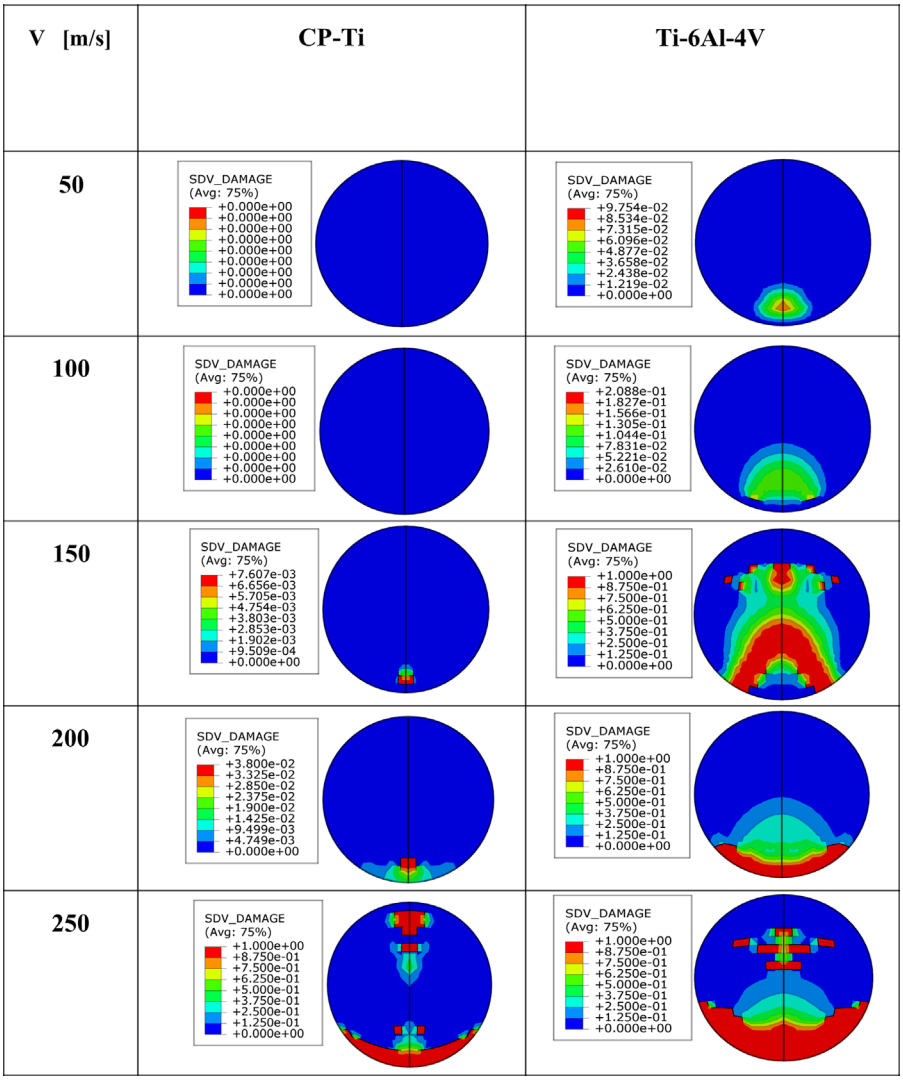

Fig. 13 – The damage in ceramic sphere at 2.5 μs after impact with the 2 plates at velocities ranging from 50 to 250 m/s. A value of 0 means no damage, while 1 means total damage.

At 250 m/s the damage is much more widespread for the case of impact with Ti–6Al–4V. This result can be rationalized by noting that Ti–6Al–4V has a much higher hardness than CP–Ti.

3.2.5. *Temperature rise in the plates due to impact*

High rate deformation of materials causes a temperature rise (thermo-mechanical coupling effect). High local temperatures

are likely to affect the mechanical properties of the material in the impacted region. Therefore, the temperature rise within the substrates was calculated using an adiabatic assumption in which all of the plastic work gets converted into heat. As such, the calculated temperatures (T) are an upper bound of the expected thermo-mechanical coupling effect. The characteristic homologous temperature T/T_m (where T_m is the melting temperature, see Table B1) reached in each material is listed in Table 3.

Table 3 shows that for the Ti–6Al–4V substrate impacted at velocities lower than 200 m/s, the temperature rise is moderate. As the impact velocity reaches and exceeds 200 m/s, the temperature rise is significant to an extent that the melting temperature is reached and even exceeded ($T/T_m \geq 1$). The melting phenomenon is likely to cause adhesion of some of the alumina debris to the impacted surface. By contrast, the temperature rise of the CP–Ti substrate is more moderate, but may nevertheless reach($T/T_m = 0.54$), which is not negligible (Fig. 14).

3.2.6. *Summary of the numerical results*

The numerical results provide a detailed characterization of the residual pressure and strain field underneath the impact. They indicate that for the specific simulated systems (particle size and target material), there is a *threshold impact velocity* (V_{th}) beyond which significant damage of the impacted plate (tearing, holes, pits, cracks) will develop. The adiabatic nature of the impact causes a high temperature rise, especially in the damaged plate areas that sustain large plastic strains. These high temperatures might cause melting, or at least significant softening of the plate material, thereby promoting embedding and adhesion of the ceramic particles to the target. Finally, the evolution of the damage in the impacting sphere is fully characterized and found to be more significant in the harder Ti–6Al–4V substrate.

Table 3 – Characteristic temperature rise (T/T_m) of the substrates CP–Ti and Ti–6Al–4V at the location site of the impact.

V [m/s]	CP–Ti [T/T_m]	Ti–6Al–4V [T/T_m]
50	0.15–0.17	0.15–0.19
100	0.15–0.19	0.15–0.21
150	0.15–0.20	0.15–0.22
200	0.31–0.42	0.55–1.16
250	0.26–0.55	0.64–1.37

4. Discussion

The present study addresses systematically the effect of grit blasting on the fatigue strength of commercial dental implants, using a combination of mechanical fatigue testing, failure analysis and numerical modeling.

The results of our study strongly suggest that the grit blasting treatment can shift from beneficial to detrimental if it is carried out in an uncontrolled manner. In the present case, the post-treatment analysis reveals tearing of the titanium/titanium alloy, which will become increasingly severe as the particle velocity increases for a given substrate. The resulting surface condition is largely affected by the particle size, particle and target mechanical properties, nozzle diameter and blasting pressure. While those parameters can be controlled to some extent, it is still important to remember that the particle velocity has an inherent statistical distribution. Those particles that impact at the higher end of the velocity spectrum are likely to cause the observed surface defects that facilitate fatigue crack initiation.

The numerical analysis reveals that for the *specific simulated treatment parameters*, a *velocity threshold* can be identified. This threshold can be used in order to evaluate the mechanical effect of the surface treatment, and define the optimal treatment parameters (particle velocity and size) that will *roughen* the surface of the implant (osseointegration) without *destroying* it (cracking).

It is important to emphasize that the numerical model which was presented is based on certain assumptions, such as adiabatic conditions and spherical shape alumina particles. In reality, the particles might be polyhedral, as shown in earlier work (Barriuso et al., 2014). We deliberately simplified the situation by adopting a spherical shape. This assumption does not detract from the absolute nature of the imparted damage, with the proviso that sharp particles might even inflict more damage than spherical ones, with an increased tendency to early particle disintegration upon impact. Another point is that the real blasting process involves impact by tens of thousands of particles of varying shape and unknown velocities. Such a situation cannot be modeled realistically, so that the current simulation addresses a single impact and its associated effects. In that sense, the obtained results are a sort of "lower bound" for the actual evolution of the implant's surface. However, it is believed that the numerical model retains the salient features of the problem at hand, namely that as the impact velocity increases, the nature and the extent of the damage vary, with the existence of a velocity threshold below which no significant damage will result from the surface treatment. It is therefore

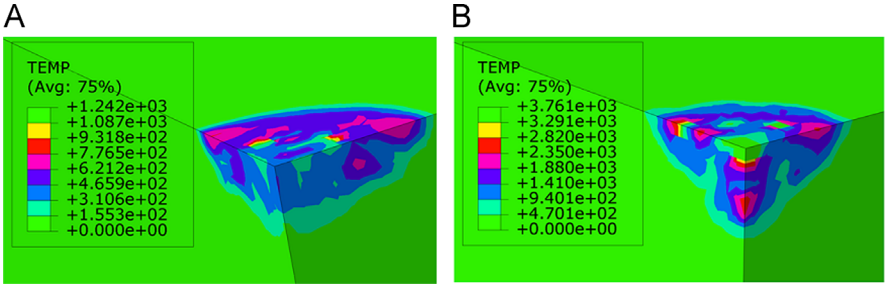

Fig. 14 – Temperature rise map (in K) for a 250 m/s impact on: A. CP–Ti, B. Ti–6Al–4V.

advised to carefully re-assess the various parameters of a planned grit-blasting treatment, simulate it to optimize it, and validate the process by performing a thorough surface characterization. At this stage, this assessment must be largely experimental.

Considering the nature of the imparted damage, SEM observations clearly showed the presence of embedded ceramic particles on the implants' surface. During the fabrication process of the implants these particles should be removed either by chemical treatments done according to the ISO recommendations (ISO B600, 2007; ISO F86, 2007), or during the etching surface treatments done using a strong acid. The very fact that these particles remained embedded to the surface, whether intact or shattered indicates that these particles have adhered to the surface as a result of the aggressive surface treatment. In that case too, the numerical simulations show that for a certain velocity, the surface temperature can approach or even exceed the melting temperature of the surface, thereby apparently promoting a strong particle-substrate adhesion process.

The embedded particles are strong stress raisers, creating a singular stress distribution in their vicinity. This singularity is created as a result of the geometry, created by the adhered particle and the different elastic properties of the metal and the ceramic (Hein and Erdogan, 1971). One can expect that the resulting "infinite" tensile stresses will generate immediate micro-cracks that can then subsequently grow by a fatigue mechanism. The embedded particles and their effect on fatigue crack nucleation were unambiguously identified for both laboratory tested and retrieved dental implants. One can now trace one of the fatigue crack initiation causes to the presence of embedded ceramic particles, a point that was not previously identified.

Finally, another misconception dealt with in this research, is that grit blasting surface treatment, with residual surface embedded particles, has no adverse effect, on both processes of osseointegration and implant surface integrity. This study shows that the treatment itself has a profound effect on the mechanical reliability of the dental implants. The main conclusion of this work is therefore that implant manufacturers and practitioners alike should be aware of the potential fatigue failure, and should take into consideration mechanical considerations related to surface preparation, in addition to the biological ones, to achieved increased mechanical reliability of dental implants.

5. Conclusion

- Potentially adverse effects of grit blasting surface treatment were shown. The Grit blasting surface treatment, if not carefully controlled, impairs the mechanical durability of dental implants.
- Both surface topography and cleanliness have a definite influence on surface cracks initiation, leading to a shorter fatigue life.
- Numerical modeling has a strong potential to improve the overall design of dental implants, with emphasis on their surface treatments.
- It is recommended to amend the standard recommendations regarding surface condition of dental implants in view of the present findings.

Acknowledgment

The authors would like to thanks Mr. A. Reuven for his assistance with the fatigue tests, and Mr. Z. Shachar helping with the scanning electron microscopy part. The authors would like to acknowledge Prof. R. Zaera for his constructive comments.

Appendix A

A. *The experimental setup and sample fixation for fatigue test*

Mechanical testing (monotonic and cyclic) was performed using an MTS servo-hydraulic load frame (MTS system, Minneapolis,

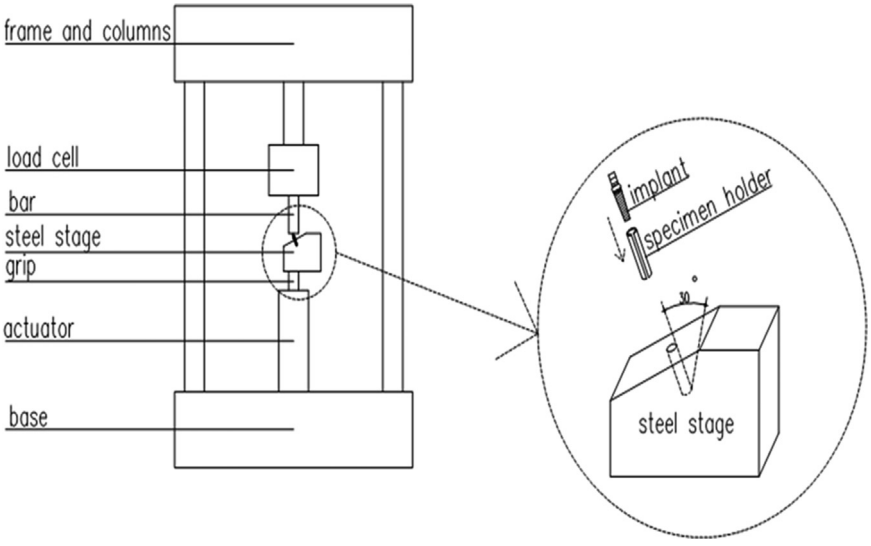

Fig. A1 – Schematic diagram of test set-up. To fix the specimen, a steel base was machined with a hole on its upper face so that the specimen so that upon insertion, the specimen would form an angle of 30°.

MN) with 250 kN load capacity, driven under load-control. Holding stage and specimen holder were made of high-strength steel. The implant was inserted into the hole of the specimen holder up to the second thread from the head of the implant. The specimen holder was then inserted to the holding stage at an angle of 30° off-axis, and fixed to the testing machine (Fig. A1). This way the testing force which was applied to the implant abutment induced a bending moment, as recommended by the ISO standard for dynamic fatigue testing for dental implants (ISO 14801, 2007). All tests were carried out at room temperature and in room air.

B. Material properties used to construct the numerical model

The elastic properties and the physical properties of CP–Ti and Ti–6Al–4V are summarized in Table B1.

The flow properties of Ti–6Al–4V, based on Rittel and Wang (2008) and Rittel et al. (2008), and of CP–Ti, based on Nemat-Nasser et al. (1999) are shown in Fig. B1.

The failure strains for positive triaxiality were based on Chen and Chiu (2005), and are shown in Fig. B2.

The JH2 material model (Johnson and Holmquist, 1994) was used for the alumina spheres (see also Holmquist et al.,

Table B1 – Elastic and physical properties of Ti–6Al–4V and CP–Ti.

Material	Modulus of elasticity [GPa]	Poisson's Ratio	Density [Kg/m^3]	Melting T	Inelastic heat fraction	Specific Heat Capacity [J/Kg–°C]
Ti–6Al–4V	114	0.33	4430	1933	0.9	526.3
CP–Ti	116	0.34	4500	1933	1	528

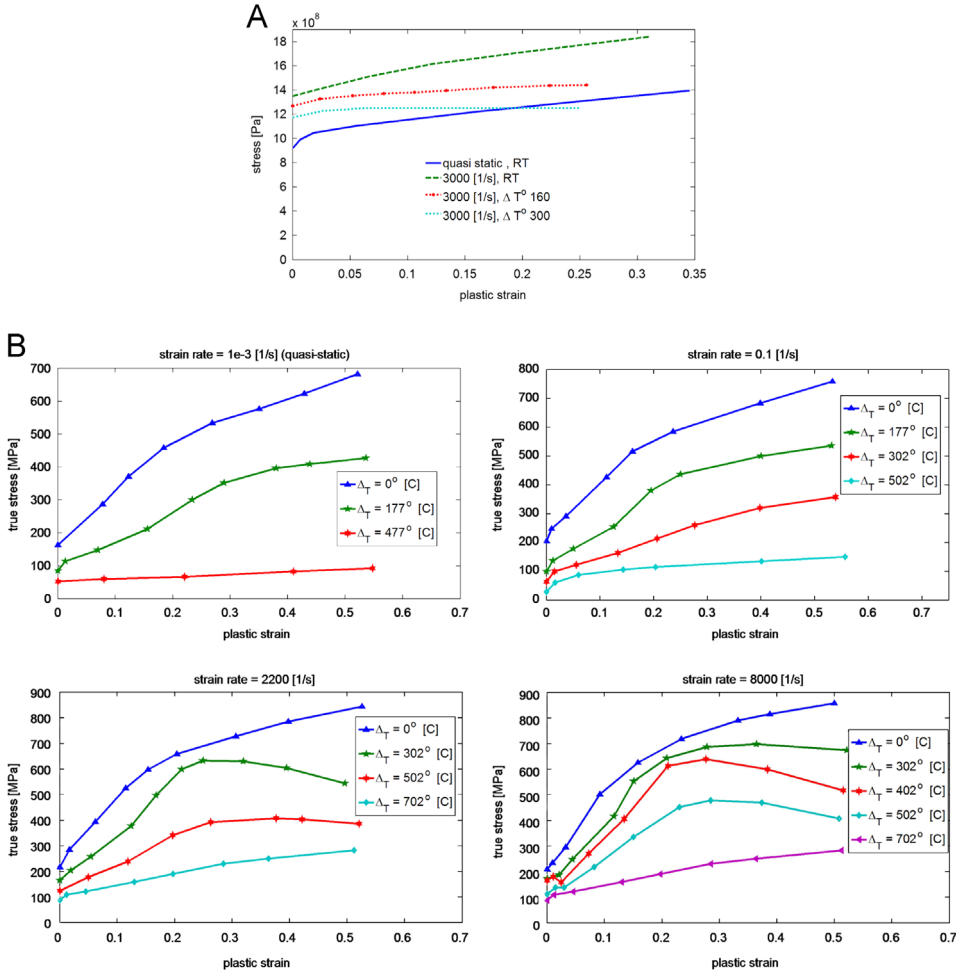

Fig. B1 – A: Flow properties of Ti–6Al–4V (from Rittel et al., 2008). B: Flow properties of CP–Ti grade 1.A : $\dot{\varepsilon} = 0.001[1/s]$ B : $\dot{\varepsilon} = 0.001[1/s]$C : $\dot{\varepsilon} = 0.001[1/s]$ D : $\dot{\varepsilon} = 0.001[1/s]$.

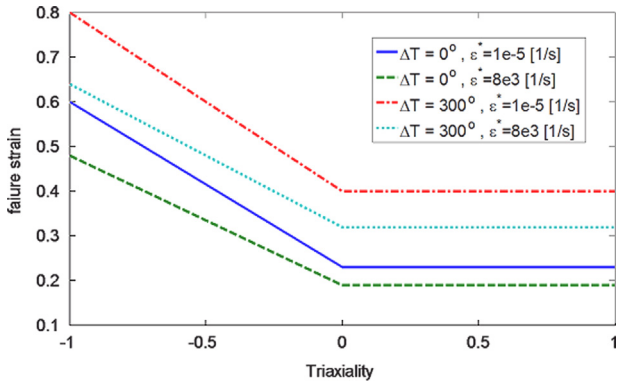

Fig. B2 – Applied failure strains versus triaxiality, temperature and strain rate.

2001). The material parameters were taken from Anderson et al. (1995).

REFERENCES

Abaqus/CAE, 2012. version 612 –2. Abaqus documentation. Abaqus analysis user's manual, Dassault systemes. Springer, New York.

Albrektsson, T., Brånemark, P.I., Hansson, H.A., Lindström, J., 1981. Osseointegrated titanium implants. Requirements for ensuring a long-lasting, direct bone-to-implant anchorage in man. Acta Orthop. Scand. 52, 155–170.

Albrektsson, T., Wennerberg, A., 2004. Oral implant surfaces: part 1-review focusing on topographic and chemical properties of different surfaces and in vivo responses to them. Int. J. Prosthodont. 17, 544–564.

Anderson, C.E., Walker, J.D., Lankford, J. 1995. Investigations of the ballistic response of brittle materials. Technical report. SwRI Project 06-5117/002, Southwest Research Institute, Materials and Structures Division, San Antonio, TX 78228-0510.

Baleani, M., Viceconti, M., Toni, A., 2000. The effect of sandblasting treatment on endurance properties of titanium alloy hip prostheses. Artif. Organs. 24, 296–299, http://dx.doi.org/10.1046/j.1525-1594.2000.06486.x).

Barriuso, S., Lieblich, M., Multigner, M., Etxeberria, I., Alberdi, A., González-Carrasco, J.L., 2011. Roughening of metallic biomaterials by abrasiveless waterjet peening: characterization and viability. Wear 270, 634–639.

Barriuso, S., Chao, J., Jimenez, J.A., Garcia, J.L., González-Carrasco, J.L., 2014. Fatigue behavior of Ti–6Al–4V and 316 LVM blasting with ceramic particles of interest for medical devices. J. Mech. Behav. Biomed. Mater. 30, 30–40.

Chen, F.K., Chiu, K.H., 2005. Stamping formability of pure titanium sheets. J. Mater. Process. Tech. 170, 181–186.

Choe, H.C., Lee, J.K., Chung, C.H., 2004. Analyses of fractured implant fixture after prolonged implantation. Met. Mater. Int. 10, 327–335.

Conforto, E., Aronsson, B.O., Salito, A., Crestou, C., Caillard, D., 2004. Rough surfaces of titanium and titanium alloys for implants and prostheses. Mat. Sci. Eng. C 24, 611–618.

Elias, C.N., Lima, J.H.C., Valiev, R., Meyers, M.A., 2008. Biomedical applications of titanium and its alloys. JOM 60, 46–49, http://dx.doi.org/10.1007/s11837-008-0031-1).

Elias, C.N., Meirelles, L., 2010. Improving osseointegration of dental implants. Expert Rev. Med. 7, 241–256, http://dx.doi.org/10.1586/erd.09.74).

Guéhennec, L.L., Soueidan, A., Layrolle, P., Amouriq, Y., 2007. Surface treatments of titanium dental implants for rapid osseointegration. Dent. Mater. 23, 844–854, http://dx.doi.org/10.1016/j.dental.2006.06.025.

Hein, V.L., Erdogan, F., 1971. Stress singularity in a two-material wedge. Int. J. Fract. Mech. 7, 317–330, http://dx.doi.org/10.1007/BF00184307.

Henley, E.J., Kumamoto, H., 1981. Reliability engineering and risk assessment. 1st edn Michigan: Prentice-Hall.

Holmquist, T.J., Templeton, D.W., Bishnoi, H.D., 2001. Constitutive modeling of aluminum nitride for large strain, high-strain rate, and high-pressure applications Int. J. Impact Eng. 25, 211–231.

ISO 14801. 2007. Fatigue test for endosseous dental implants. Geneva: international organization for standardization.

ISO B600. 2007. Surface preparation and marking of metallic surgical impalnts. Geneva: International Organization for Standardization.

ISO F86. 2007. Surface preparation and marketing of metallic surgical implants. Geneva: International Organization for Standardization.

Johnson, G.R., Holmquist, T.J., 1994. An improved computational constitutive model for brittle materials. In: Schmidt, S.C., Shaner, J.W., Samara, G.A., Ross, M. (Eds.), High Pressure Science and Technology. AIP Press, New York, pp. 981–984.

Kerlins, V., Phillips, A., 1987. Modes of Fracture, Fractography ASM Handbook. ASM International12–71.

Leinenbach, L., Eifler, D., 2006. Fatigue and cyclic deformation behavior of surface-modified titanium alloys in simulated physiological media. Biomaterials 27, 1200–1208.

Morgan, M.J., James, D.F., Pilliar, R.M., 1993. Fractures of the fixture component of an osseointegrated implant. Int. J. Oral Maxillofac. Implants 8, 409–414.

Multigner, M., Frutos, E., Mera, C.L., Chao, J., González-Carrasco, J.L., 2009. Interrogations on the sub-surface strain hardening of grit blasted Ti–6Al–4V alloy. Surf. Coat. Tech. 203, 2036–2040.

Nemat-Nasser, S., Guo, W.G., Cheng, J.Y., 1999. Mechanical properties and deformation mechanisms of commercially pure titanium. Acta Mater 47, 3705–3720.

Novovic, D. Dewes, Aspinwall, R.C., Voice, D.K., Bowen, W., 2004. The effect of machined topography and integrity on fatigue life. Int. J. Mach. Tool Manu. 44, 125–134.

Pazos, L., Corengia, P., Svoboda, H., 2010. Effect of surface treatments on the fatigue life of titanium for biomedical applications. J.Mech. Behav. Biomed. Mater. 3, 416–424.

Pjetursson, B.E., Thoma, D., Jung, R., Zwahlen, M., Zembic, A., 2012. A systematic review of the survival and complication rates of implant-supported fixed dental prostheses (FPDs) after a mean observation period of at least 5 years. Clin. Oral Implant. Res. 23, 22–38, http://dx.doi.org/10.1111/j.1600-0501.2012.02546.x.

Pommer, B., Bucur, L., Zauza, K., Tepper, G., Hof, M., Watzek, G., 2014. Meta-analysis of oral implant fracture incidence and related determinants. J. Oral Implant.

Rittel, D., Wang, Z.G., 2008. Thermo-mechanical aspects of adiabatic shear failure of AM50 and Ti6Al4V alloys. Mech. Mater. 40, 629–635.

Rittel, D., Wang, Z.G., Dorogoy, A., 2008. Geometrical imperfection and adiabatic shear banding. Int. J. Impact Eng. 35, 1280–1292.

Sbordone, L., Traini, T., Caputi, S., Scarano, A., Bortolaia, C., Piattelli, A., 2010. Scanning electron microscopy fractography analysis of fractured hollow implants. J. Oral Implantol. 36, 105–112, http://dx.doi.org/10.1563/AAID-JOI-D-10-90000).

Shemtov-Yona, K., Rittel, D., Levin, L., Machtei, E., 2014a. Effect of dental implant diameter on fatigue performance. Part I: mechanical behavior. Clin. Implant Dent. Relat. Res. 16, 172–177, http://dx.doi.org/10.1111/j.1708-8208.2012.00477.x.).

Shemtov-Yona, K., Rittel, D., Machtei, E., Levin, L., 2014b. Effect of dental implant diameter on fatigue performance. Part II: failure analysis. Clin. Implant Dent. Relat. Res. 16, 178–184, http://dx.doi.org/10.1111/j.1708-8208.2012.00476.x.

Shemtov-Yona, K., Rittel, D., 2014. Identification of failure mechanisms in retrieved fractured dental implants. Eng. Fail. Anal. 38, 58–65.

Suresh, S., 1994. Fatigue of Materials, 1st edn. Cambridge University Press, Cambridge.

Wennerberg, A., Albrektsson, T., 2009. Effects of titanium surface topography on bone integration: a systematic review. Clin. Oral Implants Res. 20 (Suppl 4), S172–S184, http://dx.doi.org/10.1111/j.1600-0501.2009.01775.x.).

Wennerberg, A., Albrektsson, T., 2010. On implant surfaces: a review of current knowledge and opinions. Int. J. Oral Maxillofac. Implants 25, 63–74.

Yokoyama, K., Ichikawa, T., Murakami, H., Miyamoto, Y., Asaoka, K., 2002. Fracture mechanisms of retrieved titanium screw thread in dental implant. Biomaterials 23, 2459–2465.